JOURNAL OF SPACECRAFT AND ROCKETS
Vol. 42, No. 6, November–December 2005

Pendulum Mode Control of Free–Free Launcher Structural Models in Gravity Fields

Sebastiaan Fransen*
ESA, 2200 AG Noordwijk, The Netherlands
Andreas Kreis†
Kreis Consultancies, CH-7212 Seewis-Dorf, Switzerland
and
Michel Klein‡
ESA, 2200 AG Noordwijk, The Netherlands

For structural models that contain tanks filled with liquid propellants subjected to gravitational forces, so-called pendulum modes exist. The same holds true for structures with prestressed elements due to gravitational forces. Depending on the sign of the eigenvalue, the pendulum mode can be classified as either stable or unstable. For launchers, the thrust point is positioned below the launcher center of gravity. Hence, unstable pendulum modes with negative eigenvalues, both due to prestress and liquid propellants, do exist. In reality, the unstable pendulum modes are controlled by thrust vectoring. In launcher–payload coupled dynamic analysis, a simple control system could be employed using control moments. The control moments can be introduced by means of a preconditioned stiffness matrix. For this purpose, the rigid-body forces or the rigid-body strain energy of the free–free stiffness matrix will be considered. A global sensing system is needed to minimize the effect of the control method on the flexible modes. The low-frequency modes are affected most by the control method. In addition to the prestress effect of gravitational forces (dead loads), the prestress effect of pressure forces (follower loads) can also be significant. The latter type of forces do not need to be controlled because they do not cause a resulting moment under rigid-body rotation.

Nomenclature

A	=	coefficient in series expansion
a	=	apparent acceleration of launcher
C	=	torsional spring stiffness, total number of c-set degrees of freedom (DOF)
D	=	number of d-set DOF
$\boldsymbol{F}$	=	excitation force vector, number of f-set DOF
f	=	frequency
g	=	Earth gravity
I	=	identity matrix, mass moment of inertia
K	=	stiffness matrix
l	=	length
M	=	mass matrix, number of m-DOF
m	=	mass
N	=	number of system n-set DOF, beam axial load
p	=	pressure
$\boldsymbol{q}, q$	=	displacement vector, variables for Lagrange equation
R	=	number of explicit rigid DOF in r-set
s	=	local coordinate along beam rigid axis
T	=	transformation matrix, thrust force, kinetic energy
t	=	local coordinate along beam rigid axis, time coordinate
u, v	=	flexible displacement
W	=	number of w-set DOF
X	=	geometric rigid-body vectors
X_R	=	rigid-body displacement in X direction
$\boldsymbol{x}$	=	displacement vector
Y_R	=	rigid-body displacement in Y direction
y	=	displacement in y direction
α, β	=	rotational stiffness term, bending stiffness
ΔP	=	pressure perturbation
θ, θ_R	=	angle of rotation, rigid-body rotation
λ	=	eigenvalue
μ	=	mass per unit length
Π	=	potential energy
ϕ	=	rigid-body vectors computed from stiffness matrix
Ψ_R	=	rigid-body rotation

Subscripts

B	=	bending
c	=	c-set DOF
ctrl	=	pendulum mode control
d	=	dry structural DOF
f	=	DOF of free fluid surface
i	=	variables defining Lagrange equation
L/V	=	launch vehicle
m	=	m-set DOF
N	=	axial force N
n	=	n-set DOF, series expansion
p	=	pendulum
r	=	r-set DOF
w	=	wet structural DOF

Superscripts

cor	=	correction
f	=	fluid model
g	=	geometric
s	=	structural model
T	=	transpose
-1	=	inverse
$'$	=	first derivative, updated value
$''$	=	second derivative

Presented as Paper 2004-1791 at the AIAA/ASME/ASCE/AHS/ASC 45th Structures, Structural Dynamics, and Materials Conference, Palm Springs, CA, 19–22 April 2004; received 8 June 2004; revision received 31 October 2004; accepted for publication 31 October 2004.

*Consultant, P.O. Box 299, AOES Group B.V.; bas.fransen@aoes.com. Professional Member AIAA.
†Consultant, Falada; andreas.kreis@akrs.ch.
‡Head, P.O. Box 299, Thermal and Structures Division; michel.klein@esa.int.

I. Introduction

A LAUNCHER that accelerates in the vertical direction experiences the reaction forces of an apparent gravity field. This apparent gravity field equates to the ratio of the total thrust and mass of the launcher, that is, T/m, and may include the Earth gravitation, that is, $T/m = a = a_{LV} + g$. For launchers with a high liquid-propellant mass, the effects of fluid sloshing in the apparent gravity field should be considered when performing a launcher coupled dynamic analysis. For this purpose, adequate fluid models shall be included in the structural model of the launcher. Application of such models generally leads to unstable pendulum modes with negative eigenvalues, depending on the thrust point position. A rigid-body rotation about an axis perpendicular to the gravity vector causes a shift of the fluid c.g., which needs to be counteracted by a control moment. To obtain zero-frequency rigid-body modes, a control moment is, therefore, needed, which, in reality, is provided by thrust vectoring or aerodynamic control forces.

For flight events with a high launcher acceleration, the prestress effect due to the apparent gravitational loads might be significant and should, therefore, be taken into account. It could affect the modal content of the launcher model and, hence, the responses found in dynamic analyses. When the prestress due to gravitational loads is taken into account, the rotational rigid-body modes about the axes perpendicular to the launcher acceleration vector become unstable pendulum modes that need to be controlled by an adequate counteracting control moment, similar to that which is required for the problem of the liquid propellants.

To avoid the complexity of an active control system by means of thrust vectoring in a coupled dynamic analysis, a new passive control system has been developed. The passive control system preconditions the launcher stiffness matrix by the addition of a control moment stiffness. The control moment stiffness is computed such that zero-frequency rigid-body modes result. To facilitate an easy formulation of the control method, so-called explicit rigid degrees of freedom are introduced that allow the subdivision of absolute motion into rigid and elastic motion. Compared to earlier work on this subject,[1] the control method outlined in this paper is based on the strain energy developed under rigid-body rotation rather than on a determinant equation. In the latter case, the determinant equation was used to solve a set of stiffness parameters on the basis of a sixfold zero root.

In addition to the prestress effect of gravitational forces (dead loads), the prestress effect of pressure forces (follower loads) can also be significant. The latter type of forces do not need to be controlled because follower forces do not cause a resulting moment under rigid-body motion. To compute the geometric stiffness for follower forces, a correction matrix is needed[2] that should be added to the classical geometric stiffness matrix. The importance of prestress due to internal pressurization (follower loads) in solid-rocket motors has been studied earlier by Christensen.[3] Prestress effects due to dead loads have not been considered before, to the present authors' knowledge.

The organization of the paper is as follows. An explanation of the transformation into explicit rigid degrees of freedom is given in Sec. II. In Sec. III, the formulation of fluid models is briefly outlined, and the associated problem of pendulum modes is explained. A discussion on geometric stiffness due to dead loads and follower loads is given in Sec. IV. In Sec. V, the pendulum mode control method is outlined. In Sec. VI, the control method is tested and physically interpreted for a free–free prestressed beam. In Sec. VII, the example of a free–free box tank filled with water is discussed. In Sec. VIII, the effects of geometric stiffness and pendulum mode control are studied for an Ariane-5 dynamic analysis. Finally, conclusions are drawn in Sec. IX.

II. Explicit Rigid Degrees of Freedom

In this section, we will consider the transformation of the equation of motion of a free–free structural system into a formulation with explicit rigid degrees (ERD) of freedom. The aim of this coordinate transformation is to split the absolute free–free motion into rigid and flexible motion. For this purpose, we first need to select a reference point (hereafter called ERD point) that will be used to describe the rigid motion. The ERD point is chosen as a loose nonstructural point. In this way, the ERD points of the various substructures that make up the launcher–payload system can be merged. Having chosen this ERD point, we can compute a set of geometric rigid-body vectors that define the rigid-body motion of all structural degrees of freedom (DOF) due to unit translations and rotations of the ERD point. In this way, the rigid-body motion of the structure can be described with respect to an inertial coordinate system (ICS), as shown in Fig. 1. For the rigid motion of the ERD point, we assume small rotations ($\theta_R \ll 1$ rad). The flexible motion can then be defined relative to the rigid motion, which is relative to a rigid reference frame (RRF), which is thought to be fixed to the ERD point. This is shown in Fig. 1.

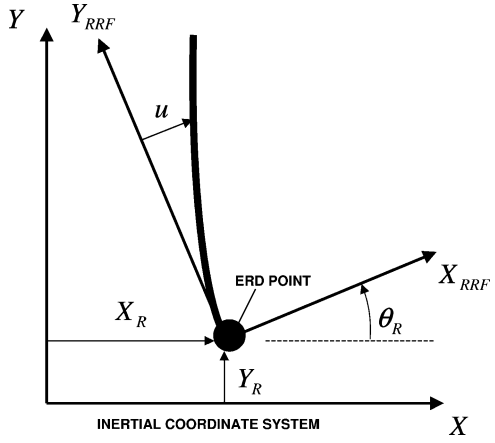

Fig. 1 Rigid and flexible motion.

The preceding procedure is given by the following coordinate transformation:

$$\bar{\boldsymbol{x}} = T\boldsymbol{q} \tag{1}$$

or

$$\bar{\boldsymbol{x}}_n = [X_{nr} \quad I_{nn}] \begin{Bmatrix} \boldsymbol{x}_r \\ \boldsymbol{x}_n \end{Bmatrix} \tag{2}$$

In this equation, $\bar{\boldsymbol{x}}_n$ is the vector of absolute displacements and $\boldsymbol{x}_n$ is the vector of flexible displacements relative to the RRF. The displacements $\boldsymbol{x}_r$ of the explicit ERD point are employed to describe the rigid-body motion of the RRF. The matrix X_{nr} consists of six geometric rigid-body vectors defined with respect to the ERD point. Next, we consider the equation of motion of a free–free structural system:

$$M\ddot{\bar{\boldsymbol{x}}} + K\bar{\boldsymbol{x}} = \boldsymbol{F} \tag{3}$$

Using Eq. (1), we can transform the equation of motion (3) as follows:

$$T^T M T\ddot{\boldsymbol{q}} + T^T K T\boldsymbol{q} = T^T \boldsymbol{F} \tag{4}$$

or

$$\tilde{M}\ddot{\boldsymbol{q}} + \tilde{K}\boldsymbol{q} = \tilde{\boldsymbol{F}} \tag{5}$$

where

$$\tilde{M} = \begin{bmatrix} X_{nr}^T M_{nn} X_{nr} & X_{nr}^T M_{nn} \\ M_{nn} X_{nr} & M_{nn} \end{bmatrix} = \begin{bmatrix} \tilde{M}_{rr} & \tilde{M}_{rn} \\ \tilde{M}_{nr} & M_{nn} \end{bmatrix} \tag{6}$$

$$\tilde{K} = \begin{bmatrix} X_{nr}^T K_{nn} X_{nr} & X_{nr}^T K_{nn} \\ K_{nn} X_{nr} & K_{nn} \end{bmatrix} = \begin{bmatrix} \tilde{K}_{rr} & \tilde{K}_{rn} \\ \tilde{K}_{nr} & K_{nn} \end{bmatrix} \tag{7}$$

For the force on the right-hand side of Eq. (5) we find

$$\tilde{\boldsymbol{F}} = \begin{Bmatrix} X_{nr}^T \boldsymbol{F}_n \\ \boldsymbol{F}_n \end{Bmatrix} = \begin{Bmatrix} \tilde{\boldsymbol{F}}_r \\ \boldsymbol{F}_n \end{Bmatrix} \tag{8}$$

The matrix $\tilde{M}_{rr}$ is the rigid-body mass matrix defined with respect to the ERD point. The forces $\tilde{F}_r$ are the applied loads projected onto the ERD point. Note that the forces $K_{nn}X_{nr} = \tilde{K}_{nr} \neq 0$ if the structural model incorporates fluid models with a free surface ($f \subset n$) subjected to gravitation. Here, n is the number of DOF of the system matrices K_{nn} and M_{nn}. The same holds true for structural models with prestressed elements due to dead loads defined at DOF $l \subseteqq n$. For structural models that do not include fluid models and/or prestressed elements due to dead loads, $K_{nn}X_{nr} = \tilde{K}_{nr} = 0$. In that case, the matrix $\tilde{K}$ takes the following form:

$$\tilde{K} = \begin{bmatrix} 0_{rr} & 0_{rn} \\ 0_{nr} & K_{nn} \end{bmatrix} \tag{9}$$

In Secs. III and IV, we will explain in more detail the physical interpretation of the forces $K_{nn}X_{nr}$ for structural models that incorporate fluid models and geometric stiffness due to dead loads, respectively. Finally, note that a set of six flexible displacements needs to be set to zero to make the system determined because the ERD transformation led to the introduction of six additional explicit rigid DOF ($R = 6$). In this way, the model gets constrained relative to the RRF in a statically determinate way. The DOF that are constrained will belong to the c set, and the remaining n-set DOF will belong to the m set ($n = c + m$). For a three-dimensional problem, $C = R = 6$, and the dimension of the system again becomes $R + N - C = R + M = N$. Thus, the nonsingular equation of motion (5) can be solved. In that case, the matrices $\tilde{M}$ and $\tilde{K}$ and the forces $\tilde{\boldsymbol{F}}$ in Eq. (5) are reduced to N size again:

$$\tilde{M} = \begin{bmatrix} \tilde{M}_{rr} & \tilde{M}_{rm} \\ \tilde{M}_{mr} & M_{mm} \end{bmatrix} \tag{10}$$

$$\tilde{K} = \begin{bmatrix} \tilde{K}_{rr} & \tilde{K}_{rm} \\ \tilde{K}_{mr} & K_{mm} \end{bmatrix} \tag{11}$$

$$\tilde{\boldsymbol{F}} = \begin{Bmatrix} \tilde{\boldsymbol{F}}_r \\ \boldsymbol{F}_m \end{Bmatrix} \tag{12}$$

III. Fluid Models

Because the liquid-propellant mass can form a substantial part of the launcher total mass, it is essential to include adequate fluid models into the structural model of the launcher to account for fluid sloshing. Usually, the contained fluids can be assumed incompressible. The respective fluid mass matrices can be derived with boundary element methods, and the fluid stiffness is obtained from the gravity potential.[4] Lately, compressible fluids models are used more frequently, and methods, have been proposed to make the formulation symmetric.[5] Here, we will focus on the treatment of symmetric models that, hence, could be either incompressible or compressible fluids. The addition of a fluid model to a structural model leads to the following type of equation of motion for the total dynamic system:

$$\begin{bmatrix} M_{dd}^s & M_{dw}^s & 0 \\ \cdot & M_{ww}^{s+f} & M_{wf}^f \\ \text{sym} & \cdot & M_{ff}^f \end{bmatrix} \begin{Bmatrix} \ddot{\tilde{\boldsymbol{x}}}_d \\ \ddot{\tilde{\boldsymbol{x}}}_w \\ \ddot{\tilde{\boldsymbol{x}}}_f \end{Bmatrix} + \begin{bmatrix} K_{dd}^s & K_{dw}^s & 0 \\ \cdot & K_{ww}^{s+f} & K_{wf}^f \\ \text{sym} & \cdot & K_{ff}^f \end{bmatrix} \begin{Bmatrix} \tilde{\boldsymbol{x}}_d \\ \tilde{\boldsymbol{x}}_w \\ \tilde{\boldsymbol{x}}_f \end{Bmatrix} = \begin{Bmatrix} \boldsymbol{F}_d \\ \boldsymbol{F}_w \\ 0 \end{Bmatrix} \tag{13}$$

In Eq. (13), the superscripts s and f denote a matrix contribution from a structural model and a fluid model, respectively. The subscripts d, w, and f indicate whether the DOF are part of the dry structure, the wet structure, or the fluid free surface, respectively. To control the pendulum modes of systems described by Eq. (13), it turns out to be advantageous (Sec. V) to transform the equation of motion into an ERD formulation according to the procedure explained in Sec. II. The ERD coordinate transformation, in line with Eqs. (1) and (2), takes the following form:

$$\begin{Bmatrix} \tilde{\boldsymbol{x}}_d \\ \tilde{\boldsymbol{x}}_w \\ \tilde{\boldsymbol{x}}_f \end{Bmatrix} = T \begin{Bmatrix} \boldsymbol{x}_r \\ \boldsymbol{x}_d \\ \boldsymbol{x}_w \\ \boldsymbol{x}_f \end{Bmatrix} \tag{14}$$

where

$$T = [X_{nr} \quad I_{nn}] = \begin{bmatrix} X_{dr} & I_{dd} & 0_{dw} & 0_{df} \\ X_{wr} & 0_{wd} & I_{ww} & 0_{wf} \\ X_{fr} & 0_{fd} & 0_{fw} & I_{ff} \end{bmatrix} \tag{15}$$

It can be shown that Eq. (13) takes the following form after ERD transformation by means of Eqs. (14) and (15):

$$\begin{bmatrix} \tilde{M}_{rr}^{s+f} & \tilde{M}_{rd}^s & \tilde{M}_{rw}^{s+f} & \tilde{M}_{rf}^f \\ \cdot & M_{dd}^s & M_{dw}^s & 0 \\ \cdot & \cdot & M_{ww}^{s+f} & M_{wf}^f \\ \text{sym} & \cdot & \cdot & M_{ff}^f \end{bmatrix} \begin{Bmatrix} \ddot{\boldsymbol{x}}_r \\ \ddot{\boldsymbol{x}}_d \\ \ddot{\boldsymbol{x}}_w \\ \ddot{\boldsymbol{x}}_f \end{Bmatrix} + \begin{bmatrix} \tilde{K}_{rr}^f & 0 & \tilde{K}_{rw}^f & \tilde{K}_{rf}^f \\ \cdot & K_{dd}^s & K_{dw}^s & 0 \\ \cdot & \cdot & K_{ww}^{s+f} & K_{wf}^f \\ \text{sym} & \cdot & \cdot & K_{ff}^f \end{bmatrix} \begin{Bmatrix} \boldsymbol{x}_r \\ \boldsymbol{x}_d \\ \boldsymbol{x}_w \\ \boldsymbol{x}_f \end{Bmatrix} = \begin{Bmatrix} \tilde{\boldsymbol{F}}_r \\ \boldsymbol{F}_d \\ \boldsymbol{F}_w \\ \boldsymbol{0} \end{Bmatrix} \tag{16}$$

where

$$\tilde{M}_{rr}^{s+f} = X_{nr}^T M_{nn} X_{nr} \tag{17}$$

$$\tilde{M}_{rd}^s = \left[M_{dd}^s X_{dr} + M_{dw}^s X_{wr} \right]^T \tag{18}$$

$$\tilde{M}_{rw}^{s+f} = \left[M_{wd}^s X_{dr} + M_{ww}^{s+f} X_{wr} + M_{wf}^f X_{fr} \right)\Big]^T \tag{19}$$

$$\tilde{M}_{rf}^f = \left[M_{fw}^f X_{wr} + M_{ff}^f X_{fr} \right)\Big]^T \tag{20}$$

$$\tilde{\boldsymbol{F}}_r = X_{nr}^T \boldsymbol{F}_n \tag{21}$$

In Eq. (17), M_{nn} is the mass matrix of the complete substructure with fluid included, and, therefore, it is equal to the complete mass matrix in Eq. (13). Hence, $N = D + W + F$. Furthermore, $\boldsymbol{F}_n$ in Eq. (21) is the complete load vector as given on the right-hand side in Eq. (13). As observed from Eqs. (17–21), the ERD mass matrix partitions are obtained from the usual ERD transformation as explained in Sec. II. The ERD coupling matrices associated with the fluid stiffness matrix must be defined by special fluid modelling tools such as fluid analysis by boundary elements (FABE).[6] The structural matrices can be generated by any finite element package and are ERD-transformed before the addition of the ERD-transformed fluid matrices. The matrix $\tilde{K}_{rr}^f$ has the form as given by Eq. (22) and is associated with the pendulum modes as will be shown in Sec. V:

$$\tilde{K}_{rr}^f = \begin{bmatrix} 0 & 0 & 0 & 0 & 0 & 0 \\ \cdot & 0 & 0 & 0 & 0 & 0 \\ \cdot & \cdot & 0 & 0 & 0 & 0 \\ \cdot & \cdot & \cdot & \alpha_x & \alpha_{xy} & 0 \\ \cdot & \cdot & \cdot & \cdot & \alpha_y & 0 \\ \text{sym} & \cdot & \cdot & \cdot & \cdot & 0 \end{bmatrix} \tag{22}$$

The rigid-body rotations about the lateral axes cause a movement of the fluid c.g. in a sideward direction (Fig. 2). Depending on the

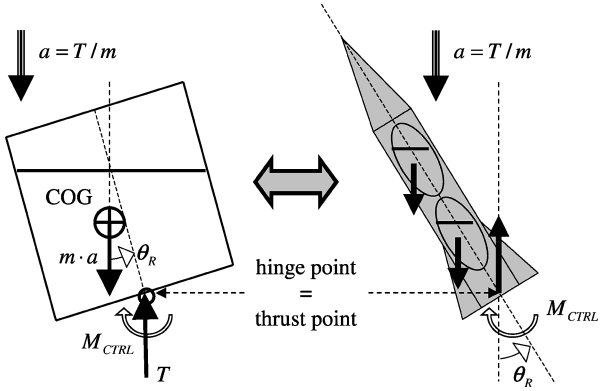

Fig. 2 Pendulum mode, controlled.

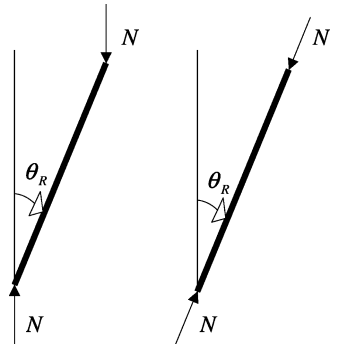

Fig. 3 Dead and follower loads.

thrust point (hinge point) position, such rigid-body rotations will result in a stable, neutral, or unstable system. In the latter case, a control moment is needed to equilibrate the resulting moment, which tends to increase the rotation angle (Fig. 2). Because the free surface remains horizontal, that is, perpendicular to the gravity vector, the fluid motion can indeed be said to be rigid. As shown in Fig. 2, the unstable pendulum mode for the free–free square tank corresponds to the pendulum modes found for free–free launcher structures with liquid propellants because the thrust point of the launcher (hinge point) is located below the c.g. of the liquid propellants.

IV. Geometric Stiffness

For launch vehicles subjected to an apparent acceleration $a = T/m$, the prestress effects of the compressive loads can be substantial and will depend on the magnitude of acceleration. The same holds true for tank structures loaded by a high-pressure differential. In those cases, the geometric stiffness shall be superimposed to the structural stiffness matrix. As a consequence of the increased or decreased stiffness, the launch vehicle eigenfrequencies might be affected, as was also found in a study performed by Christensen.[3]

The treatment of geometric stiffness due to dead loads and follower loads is different, and, hence, the loads should be classified as either dead loads or follower loads. Dead loads are defined as loads that are invariant to rigid-body rotations as well as to structural deformation, both in terms of magnitude and direction. Such loads keep the same orientation with respect to the inertial coordinate system. As an example, we mention Earth gravitation forces. The thrust, and, as a consequence the forces due to the apparent acceleration $a = T/m$, are also considered dead loads in launcher–payload coupled dynamic analysis. Note that Earth gravity can be part of the apparent acceleration $T/m = a_{L/V} + g$. On the contrary, we define follower loads as loads that follow the rigid-body rotations and structural deformation of the structure. Typical follower loads are differential pressure loads in tanks. Clearly, the dead loads will cause residual moments about the thrust application point when the launch vehicle is subjected to rigid rotations. For follower loads, this problem does not exist. This is shown in Fig. 3.

A. Dead Loads

The addition of the geometric stiffness yields the following equation of motion:

$$M\ddot{\bar{x}} + (K + K^g)\bar{x} = F \tag{23}$$

If K^g is the geometric stiffness matrix due to dead loads, the ERD transformation of Eq. (23) leads to the following equation of motion:

$$\begin{bmatrix} X_{nr}^T M_{nn} X_{nr} & X_{nr}^T M_{nn} \\ M_{nn} X_{nr} & M_{nn} \end{bmatrix} \begin{Bmatrix} \ddot{x}_r \\ \ddot{x}_n \end{Bmatrix} + \begin{bmatrix} X_{nr}^T K_{nn}^g X_{nr} & X_{nr}^T K_{nn}^g \\ K_{nn}^g X_{nr} & K_{nn} + K_{nn}^g \end{bmatrix} \begin{Bmatrix} x_r \\ x_n \end{Bmatrix} = \begin{Bmatrix} X_{nr}^T F_n \\ F_n \end{Bmatrix} \tag{24}$$

The term $K_{nn}^g X_{nr}$ can be defined as the residual forces due to rigid-body motion. The residual forces $K_{nn}^g X_{nr}$ are zero for translational rigid-body modes. For the rotational rigid-body modes, we find nonzero residual forces that are actually the sine components of the rotated prestress forces. The term $X_{nr}^T K_{nn}^g X_{nr}$ contains the residual moments due to the forces $K_{nn}^g X_{nr}$ about the ERD point. Because of the moments created by the residual forces, the rotational rigid-body modes will be unstable and need to be controlled to obtain zero-frequency rigid-body modes suited for free–free coupled dynamic analysis.

To illustrate more clearly the physical meaning of the residual forces $K_{nn}^g X_{nr}$ and moments $X_{nr}^T K_{nn}^g X_{nr}$, let us consider the geometric stiffness matrix for the beam element under compression as shown in the upper part of Fig. 4. The geometric stiffness matrix for such a beam element[7] is given by

$$K^g = -\frac{N}{30l} \begin{bmatrix} 36 & 3l & -36 & 3l \\ 3l & 4l^2 & -3l & -l^2 \\ -36 & -3l & 36 & -3l \\ 3l & -l^2 & -3l & 4l^2 \end{bmatrix} \tag{25}$$

Indeed, the geometric stiffness matrix is only a function of the geometry of the element and the applied loads. The associated DOF

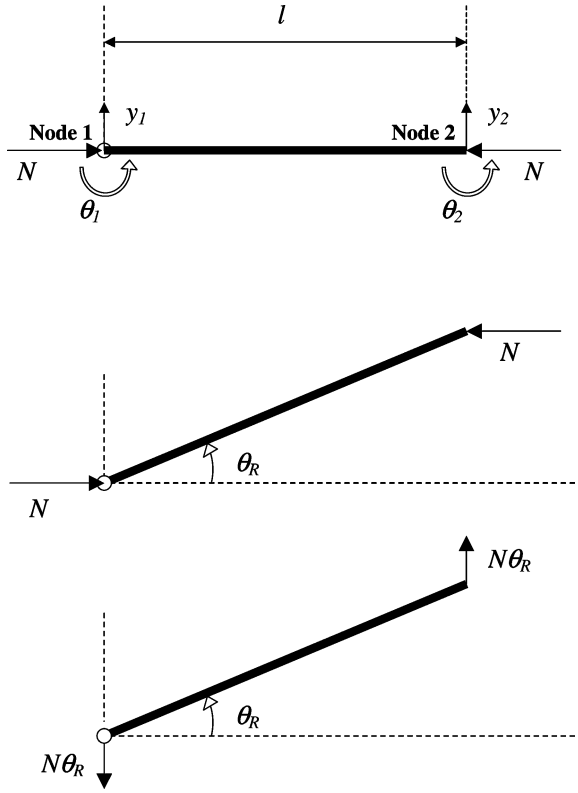

Fig. 4 Beam element loaded by compressive forces.

are given by the following vector:

$$\bar{\boldsymbol{x}} = \begin{Bmatrix} y_1 \\ \theta_1 \\ y_2 \\ \theta_2 \end{Bmatrix} \tag{26}$$

One can easily verify that a rigid-body rotation θ_R about node 1 yields the following residual force vector:

$$K^g \bar{\boldsymbol{x}} = K^g_{nn} X_{nr} = -\frac{N}{30l} \begin{bmatrix} 36 & 3l & -36 & 3l \\ 3l & 4l^2 & -3l & -l^2 \\ -36 & -3l & 36 & -3l \\ 3l & -l^2 & -3l & 4l^2 \end{bmatrix} \begin{Bmatrix} 0 \\ \theta_R \\ \theta_R l \\ \theta_R \end{Bmatrix}$$

$$= \begin{Bmatrix} N\theta_R \\ 0 \\ -N\theta_R \\ 0 \end{Bmatrix} \tag{27}$$

The equation of motion, including the effect of prestress, is given by Eq. (23). If we consider the forces $K^g \bar{\boldsymbol{x}}$ as applied loads, we can write

$$M\ddot{\bar{x}} + K\bar{\boldsymbol{x}} = \boldsymbol{F} - K^g \bar{\boldsymbol{x}} \tag{28}$$

The residual forces $-K^g \bar{\boldsymbol{x}} = -K^g_{nn} X_{nr}$ are shown in the lower part of Fig. 4 and yield the same destabilizing moment as the force couple N (middle part of Fig. 4). This moment is called the residual moment and can be obtained from the computation of the matrix $X^T_{nr} K^g_{nn} X_{nr}$, as further outlined hereafter by the ERD transformation of K^g.

The transformation matrix T, as given by Eqs. (1) and (2), has the following form for this two-dimensional case:

$$T = [X_{nr} \quad I_{nn}] \tag{29}$$

where

$$X_{nr} = \begin{bmatrix} 1 & 0 \\ 0 & 1 \\ 1 & l \\ 0 & 1 \end{bmatrix} \tag{30}$$

Hence, we find

$$T^T K^g_{nn} T = \begin{bmatrix} X^T_{nr} K^g_{nn} X_{nr} & X^T_{nr} K^g_{nn} \\ K_{nn} X_{nr} & K^g_{nn} \end{bmatrix} = \begin{bmatrix} \tilde{K}_{rr} & \tilde{K}_{rn} \\ \tilde{K}_{nr} & K^g_{nn} \end{bmatrix}$$

$$= -\frac{N}{30l} \left[\begin{array}{cc:cccc} 0 & 0 & 0 & 0 & 0 & 0 \\ 0 & 30l^2 & -30l & 0 & 30l & 0 \\ \hdashline \cdots & \cdots & \cdots & \cdots & \cdots & \cdots \\ 0 & -30l & 36 & 3l & -36 & 3l \\ 0 & 0 & 3l & 4l^2 & -3l & -l^2 \\ 0 & 30l & -36 & -3l & 36 & -3l \\ 0 & 0 & 3l & -l^2 & -3l & 4l^2 \end{array}\right] \tag{31}$$

Furthermore, we can see that the matrix $\tilde{K}_{rr}$ has the following form:

$$\tilde{K}_{rr} = X^T_{nr} K^g_{nn} X_{nr} = \begin{bmatrix} 0 & 0 \\ 0 & \alpha \end{bmatrix} \tag{32}$$

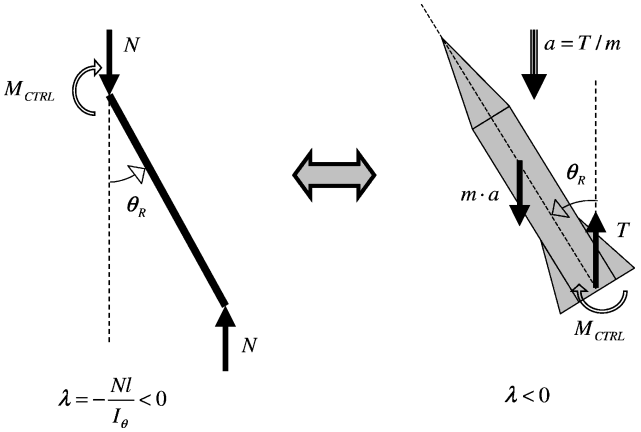

Fig. 5 Analogy between beam and rocket dead loads.

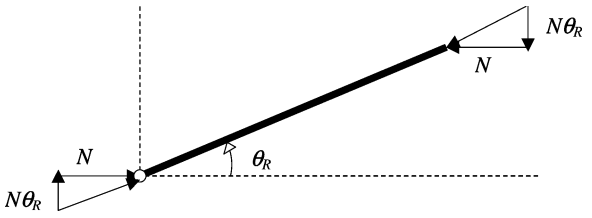

Fig. 6 Correction forces.

where

$$\alpha = -Nl \tag{33}$$

The residual moment Nl results from the dead loads N under a unit rigid-body rotation. In Fig. 4, $\theta_R = 1$ rad. The analogy between a free–free beam and a rocket subjected to compressive loads is shown in Fig. 5. In both cases, the eigenvalue will be less than zero because of the instability caused by the moment Nl. To enforce zero-frequency rigid-body modes a control moment is needed.

B. Follower Loads

As mentioned earlier, the residual moment due to a rigid-body rotation of a beam prestressed by follower loads shall be zero. The forces computed in Eq. (27) for a rigid-body rotation should, therefore, become zero when we consider follower loads. Hence, note that a correction matrix is needed that has to be superimposed to K^g. The correction matrix for the beam element shown in Fig. 4 has the following form:

$$K^{\text{cor}} = -N \begin{bmatrix} 0 & 1 & 0 & 0 \\ 0 & 0 & 0 & 0 \\ 0 & 0 & 0 & -1 \\ 0 & 0 & 0 & 0 \end{bmatrix} \tag{34}$$

By the use of Eq. (34), it is easily verified that

$$[K^g + K^{\text{cor}}] \begin{Bmatrix} 0 \\ \theta_R \\ \theta_R l \\ \theta_R \end{Bmatrix} = \begin{Bmatrix} 0 \\ 0 \\ 0 \\ 0 \end{Bmatrix} \tag{35}$$

The matrix K^{cor} yields forces in the y direction that make the dead load a follower load, as shown in Fig. 6. Clearly, no control moment is needed. Note that the correction matrix is nonsymmetric. In the literature, we find various names for the correction matrix K^{cor}, such as follower force matrix[2] or pressure stiffness matrix.[3] Usually, follower forces are associated with internal pressure loads in tank structures. For such closed volumes, note that the correction matrix K^{cor} becomes symmetric.[2]

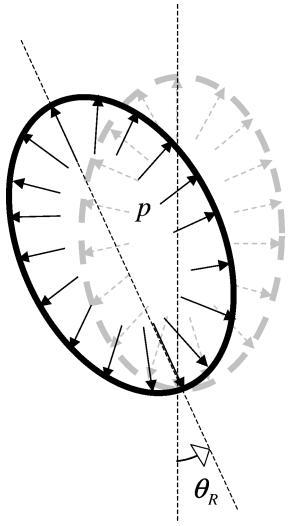

Fig. 7 Follower pressure load in closed tank.

The ERD-transformed equation of motion for systems with geometric stiffness due to follower forces will generally have the following form:

$$\begin{bmatrix} X_{nr}^T M_{nn} X_{nr} & X_{nr}^T M_{nn} \\ M_{nn} X_{nr} & M_{nn} \end{bmatrix} \begin{Bmatrix} \ddot{\boldsymbol{x}}_r \\ \ddot{\boldsymbol{x}}_n \end{Bmatrix} + \begin{bmatrix} 0 & X_{nr}^T \left(K_{nn}^g + K_{nn}^{\text{cor}} \right) \\ 0 & K_{nn} + K_{nn}^g + K_{nn}^{\text{cor}} \end{bmatrix} \begin{Bmatrix} \boldsymbol{x}_r \\ \boldsymbol{x}_n \end{Bmatrix} = \begin{Bmatrix} X_{nr}^T \boldsymbol{F}_n \\ \boldsymbol{F}_n \end{Bmatrix} \tag{36}$$

Only in the case of a symmetric correction matrix K^{cor}, that is, for pressurized volumes closed internally, do we find a symmetric formulation of the stiffness matrix in the equation of motion:

$$\begin{bmatrix} X_{nr}^T M_{nn} X_{nr} & X_{nr}^T M_{nn} \\ M_{nn} X_{nr} & M_{nn} \end{bmatrix} \begin{Bmatrix} \ddot{\boldsymbol{x}}_r \\ \ddot{\boldsymbol{x}}_n \end{Bmatrix} + \begin{bmatrix} 0 & 0 \\ 0 & K_{nn} + K_{nn}^g + K_{nn}^{\text{cor}} \end{bmatrix} \begin{Bmatrix} \boldsymbol{x}_r \\ \boldsymbol{x}_n \end{Bmatrix} = \begin{Bmatrix} X_{nr}^T \boldsymbol{F}_n \\ \boldsymbol{F}_n \end{Bmatrix} \tag{37}$$

In this paper, we will presume symmetric correction matrices and, hence, pressurized structures that are closed, as shown in Fig. 7.

V. Control of Pendulum Modes

In Sec. IV.A, we saw that the matrix $\tilde{K}_{rr}$ contains the residual moment(s) about the ERD point when the structure contains elements prestressed by dead loads. [Refer to Eq. (32).] In a similar fashion, Eq. (22) contains the residual moments about the ERD point for structures that contain fluids subjected to gravity. To control the pendulum modes of these type of structures, that is, to shift the negative eigenvalues to zero, it now seems obvious to add local stiffness on the ERD point rotational DOF of the matrix $\tilde{K}_{rr}$. This corresponds to the application of control moments as shown in Figs. 2 and 5, which mimic the action of control forces used in reality.

The aim of the pendulum mode control method is, thus, the modification of the matrix partition $\tilde{K}_{rr}$ of the ERD-transformed stiffness matrix, such that zero-frequency rigid-body modes are obtained. An elegant way to perform this modification is to consider the forces or the strain energy of the system due to rigid-body motion because both quantities shall be zero. To compute the rigid-body forces or rigid-body strain energy, we first need to solve the geometric rigid-body modes due to unit displacements of the ERD point (r-set DOF).

We now consider two systems, one excluding and one including dead load prestress effects and/or fluids subjected to gravity:

1) We first consider a system excluding dead load prestress effects and/or fluids subjected to gravity. In this case, the true rigid-body modes of the system are given by

$$\bar{\boldsymbol{x}}_{nr} = X_{nr} \tag{38}$$

which, by definition, satisfy $K_{nn} X_{nr} = 0$ if K_{nn} is the basic linear stiffness matrix. In the ERD-transformed coordinates, the rigid-body modes are, according to Eqs. (1) and (2),

$$q = \begin{Bmatrix} I_{rr} \\ 0_{nr} \end{Bmatrix} \tag{39}$$

If we constrain six DOF to the rigid reference frame to make the system nonsingular (cf. Sec. II), we obtain the following rigid-body modes ($M + R = N$):

$$q = \begin{Bmatrix} I_{rr} \\ 0_{mr} \end{Bmatrix} \tag{40}$$

2) We now consider a system including dead load prestress effects and/or fluids subjected to gravity. In this case, $K_{nn} X_{nr} = \tilde{K}_{nr} \neq 0$ and $X_{nr}^T K_{nn} X_{nr} = \tilde{K}_{rr} \neq 0$, and the rigid-body modes are solved from the following equation, in which the N–M size-reduced ERD-transformed stiffness matrix (11) is used:

$$\begin{bmatrix} \tilde{K}_{rr} & \tilde{K}_{rm} \\ \tilde{K}_{mr} & K_{mm} \end{bmatrix} \begin{bmatrix} I_{rr} \\ \phi_{mr} \end{bmatrix} = \begin{bmatrix} F_{rr} \\ 0_{mr} \end{bmatrix} \tag{41}$$

Now, the rigid-body modes follow from the second row partition:

$$\phi_{mr} = -K_{mm}^{-1} \tilde{K}_{mr} \tag{42}$$

and, thus,

$$q = \begin{Bmatrix} I_{rr} \\ \phi_{mr} \end{Bmatrix} \tag{43}$$

The rigid-body forces are given by F_{rr}.

Note that in the case where $K_{mr} = 0$ and $K_{rr} = 0$, that is, the system excludes dead load prestress effects and/or fluids subjected to gravity, the rigid-body modes that would follow from Eq. (41) are indeed given by Eq. (40). Hence, the flexible displacements $\phi_{mr} = 0$ and the reaction forces $F_{rr} = 0$, as should be the case for true rigid-body modes in ERD formulation.

For systems including dead load prestress effects and/or fluids subjected to gravity, $K_{mr} \neq 0$ and $K_{rr} \neq 0$, and, in that case, the term $\phi_{mr} \neq 0$ as can be seen from Eq. (42). It also means that the reaction forces F_{rr}, or, more precisely, the moments in F_{rr}, will not be zero. To have a free–free system, these forces shall be zero such that $\tilde{K} q = 0$. From the first row partition of Eq. (41), we then find for the modified matrix $\tilde{K}'_{rr}$

$$\tilde{K}'_{rr} = -\tilde{K}_{rm} \phi_{mr} \tag{44}$$

An alternative way to find this solution for $\tilde{K}'_{rr}$ is to require that the system does not develop any strain energy under the rigid-body motion given by Eq. (43). The strain energy can be formulated as follows for the ERD-transformed stiffness matrix,

$$\frac{1}{2} \begin{bmatrix} I_{rr} & \phi_{mr}^T \end{bmatrix} \begin{bmatrix} \tilde{K}_{rr} & \tilde{K}_{rm} \\ \tilde{K}_{mr} & K_{mm} \end{bmatrix} \begin{bmatrix} I_{rr} \\ \phi_{mr} \end{bmatrix} = E_{rr} \tag{45}$$

where E_{rr} is a 6×6 rigid-body strain matrix with the following structure:

$$E_{rr} = \begin{bmatrix} 0 & 0 & 0 & 0 & 0 & 0 \\ \cdot & 0 & 0 & 0 & 0 & 0 \\ \cdot & \cdot & 0 & 0 & 0 & 0 \\ \cdot & \cdot & \cdot & \alpha_x & \alpha_{xy} & 0 \\ \cdot & \cdot & \cdot & \cdot & \alpha_y & 0 \\ \text{sym} & \cdot & \cdot & \cdot & \cdot & 0 \end{bmatrix} \tag{46}$$

The values for the rotations are the strain energy rates (or moments) that result from unit rigid-body rotations of the ERD point. The z

direction has been assumed to be the gravity direction. To enforce the strain energy to zero, we will write Eq. (45) as

$$\tfrac{1}{2}\left(\phi_{mr}^T K_{mm}\phi_{mr} + \phi_{mr}^T \tilde{K}_{mr} + \tilde{K}_{rm}\phi_{mr} + \tilde{K}_{rr}\right) = E_{rr} \tag{47}$$

Because of symmetry, Eq. (47) can be written as

$$\tfrac{1}{2}\left(\phi_{mr}^T K_{mm}\phi_{mr} + 2\phi_{mr}^T \tilde{K}_{mr} + \tilde{K}_{rr}\right) = E_{rr} \tag{48}$$

Next, we enforce $E_{rr} = 0$ and solve for $\tilde{K}'_{rr}$. In that case, we obtain

$$\tfrac{1}{2}\left(\phi_{mr}^T K_{mm}\phi_{mr} + 2\phi_{mr}^T \tilde{K}_{mr} + \tilde{K}'_{rr}\right) = 0$$

$$\Rightarrow\ \tilde{K}'_{rr} = -\phi_{mr}^T K_{mm}\phi_{mr} - 2\phi_{mr}^T \tilde{K}_{mr} \tag{49}$$

Using Eq. (42), we can simplify Eq. (49) to Eq. (44). The stiffness matrix is now updated by replacing the old matrix $\tilde{K}_{rr}$ with the updated $\tilde{K}'_{rr}$:

$$\tilde{K}' = \begin{bmatrix} \tilde{K}'_{rr} & \tilde{K}_{rm} \\ \tilde{K}_{mr} & \tilde{K}_{mm} \end{bmatrix} \tag{50}$$

The old and updated matrix $\tilde{K}_{rr}$ have the same structure,

$$\tilde{K}_{rr} = \begin{bmatrix} 0 & 0 & 0 & 0 & 0 & 0 \\ \cdot & 0 & 0 & 0 & 0 & 0 \\ \cdot & \cdot & 0 & 0 & 0 & 0 \\ \cdot & \cdot & \cdot & \alpha_x & \alpha_{xy} & 0 \\ \cdot & \cdot & \cdot & \cdot & \alpha_y & 0 \\ \text{sym} & \cdot & \cdot & \cdot & \cdot & 0 \end{bmatrix} \tag{51}$$

By means of the updated stiffness matrix $\tilde{K}_{rr}$, found by either the rigid-body force method or the rigid-body strain energy method, the rigid-body modes computed with an eigenvalue solver will be shifted to zero-frequency rigid-body modes. The new pendulum mode control method is simple and robust, yielding controlled zero-frequency rigid-body modes on the order of 10^{-6} Hz for all rotations when the Lanczos eigensolver is adopted. For the determinant method,[1] the controlled rigid-body mode eigenfrequencies were found to be in the order of 10^{-2} Hz when the method was applied to larger systems. Only for very small problems were no differences in accuracy found.

VI. Choice of the *c*-Set DOF or Sensor Locations

By means of a simple example problem of a prestressed beam, we will show how the pendulum mode control method as outlined in Sec. V can be physically interpreted. Special attention will be devoted to the choice of the c-set DOF, which are constrained to the rigid reference frame to make the ERD-transformed system nonsingular. For this purpose, two benchmark problems have been defined (Fig. 8), for which semi-analytical solutions can be developed. In fact, the two benchmark problems constitute the same problem, except for the choice of the c-set ($n = m + c$) if pendulum mode control is activated. In that case, the eigensolutions for the two benchmarks may differ because the control matrix $\tilde{K}'_{rr}$ as given by Eq. (44) depends on the choice of the c-set.

The semi-analytical solutions for the two benchmark problems in Fig. 8 can be compared with the solutions generated for corresponding finite element (FE) models. For the semi-analytical cases the pendulum mode will be controlled by an adequately chosen control moment that is applied to the RRF. The control moment is determined by trial and error until a zero-frequency rotational rigid-body mode is obtained. For the control of the FE models, the control method, as outlined in Sec. V, will be adopted. The beam FE models consist of 10 simple beam element connections (CBAR[8] elements). It will be shown that the eigensolutions obtained with the semi-analytical method and FE method are in close proximity.

The choice of DOF for the two benchmark problems is as follows:

1) For benchmark 1, variables θ_R and Y_R describe the motion of the RRF, and $u(s)$ describes the motion of the beam relative to the reference frame. The beam is simply supported to the RRF at both ends [c-set DOF, $u(s=0) = 0$, and $u(s=l) = 0$].

2) For benchmark 2, variables Ψ_R and Y_R describe the motion of the RRF (r-set DOF), and $u(s)$ describes the motion of the beam relative to the reference frame of benchmark 1 (n-set DOF). The beam is clamped to the RRF at the upper end [c-set DOF, $u(s = 0) = 0$ and $u'(s=0) = \Psi_R - \theta_R$].

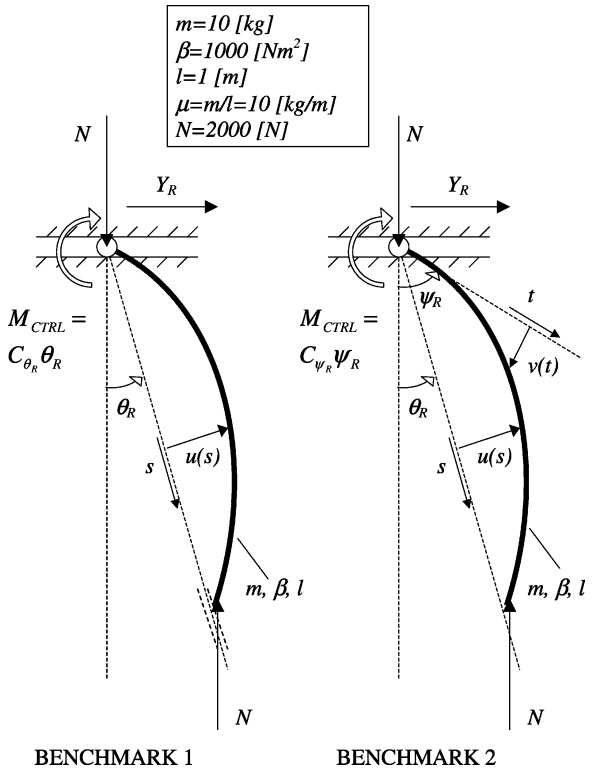

Fig. 8 Benchmark problems.

The relation between the rigid rotation of the two reference frames is, thus, given by

$$\theta_R = \Psi_R - u'(s=0) \tag{52}$$

where we assume small rotations,

$$\theta_R,\ \Psi_R,\ u'(s=0) \ll 1 \tag{53}$$

In both examples, a control moment, proportional to θ_R and Ψ_R, respectively, is applied at the upper end of the reference frame. The control moment is thought to be generated by a torsional spring with a torsional spring stiffness C_{θ_R} and C_{Ψ_R}, respectively, as indicated in Fig. 8. The semi-analytical solutions are based on a series expansion of $u(s)$:

$$u(s) = \sum_{n=1}^{\infty} A_n \sin(n\pi s/l) \tag{54}$$

The expressions for kinetic and potential energies are solved, and the equations of motion are derived using Lagrange equations. For benchmark 1, the following kinetic and potential energies can be derived for kinetic energy,

$$T = \frac{\mu}{2}\int_0^l [\dot{Y}_R + s\dot{\theta}_R + \dot{u}(s)]^2\,\mathrm{d}s \tag{55}$$

for potential energy due to bending,

$$\Pi_B = \frac{\beta}{2}\int_0^l [u''(s)]^2\,\mathrm{d}s \tag{56}$$

for potential energy due to M_{ctrl},

$$\Pi_{\text{ctrl}} = \tfrac{1}{2} C_{\theta_R} \theta_R^2 \tag{57}$$

for potential energy due to N,

$$\Pi_N = \frac{1}{2} N l \theta_R^2 + \frac{1}{2} N \int_0^l [u'(s)]^2 \, \mathrm{d}s \tag{58}$$

for total potential energy,

$$\Pi = \Pi_B + \Pi_{\text{ctrl}} + \Pi_N \tag{59}$$

and for the equation of motion from the Lagrange equation

$$\frac{\partial}{\partial t} \frac{\partial T}{\partial \dot{q}_i} + \frac{\partial \Pi}{\partial q_i} = 0 \tag{60}$$

where the variables q_i are given by

$$q_i = (A_n, Y_R, \theta_R) \tag{61}$$

Similar expressions can be derived for benchmark 2, by substituting Eq. (52) into the expressions for the kinetic energy Eq. (55) and the potential energy Eq. (58), and by replacing θ_R with Ψ_R in the control moment energy given by Eq. (57). In that case, the equation of motion is developed for the variables,

$$q_i = (A_n, Y_R, \Psi_R) \tag{62}$$

It is easily verified that, for a rigid free–free beam, the pendulum frequency is given by

$$\omega_R^2 = \lambda_p = Nl/I_\theta = Nl/(1/12)ml^2 \tag{63}$$

Note that for $N < 0$ (compression), the pendulum eigenvalue $\lambda_p < 0$, denoting instability. For the benchmark problems, we find $\lambda_p = -2400$ rad^2/s^2, using the beam properties and compression force value as indicated in Fig. 8. The corresponding pendulum eigenfrequency, defined as $f_R = 1/2\pi\sqrt{|\lambda_p|}$, equates to 7.7970 Hz. In Tables 1 and 2, the eigenfrequency results are tabulated for benchmarks 1 and 2, respectively. The semi-analytical (SA) results were computed for $n = 1, \ldots, 100$ in the series expansion. The results obtained with the FE models are given for the controlled analysis only. Because of the compressive loads, the bending eigenfrequencies decrease (third column of Tables 1 and 2).

Table 1 Eigenfrequencies: benchmark 1

	f, Hz			
		$N = 2000$ N		
Mode no./type	$N = 0$ N, SA	No control SA	Control SA	Control FE
1/R	0.00	7.84	0.00	0.00
2/R	0.00	0.00	0.00	0.00
3/B	35.61	31.88	31.88	31.88
4/B	98.16	95.30	95.72	95.74
5/B	192.42	189.95	189.95	190.12
6/B	318.09	315.81	315.94	316.70
7/B	475.17	473.02	473.02	475.42
8/B	663.66	661.60	661.66	667.79

Table 2 Eigenfrequencies: benchmark 2

	f, Hz			
		$N = 2000$ N		
Mode no./type	$N = 0$ N, SA	No control SA	Control SA	Control FE
1/R	0.00	7.84	0.00	0.00
2/R	0.00	0.00	0.00	0.00
3/B	35.61	31.88	41.60	41.60
4/B	98.16	95.30	108.13	108.16
5/B	192.42	189.95	205.01	205.24
6/B	318.09	315.81	332.63	333.54
7/B	475.17	473.02	491.22	493.96
8/B	663.66	661.60	680.90	687.71

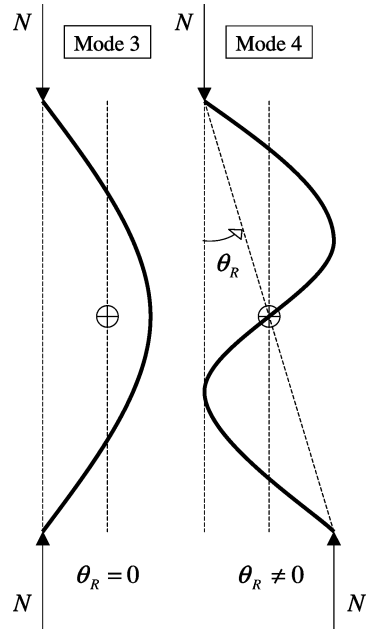

Fig. 9 Mode shapes.

In benchmark 1, there is no interaction of the control moment with the deformation of the beam, and the eigenfrequencies are only minimally increased for those modes where θ_R is not equal to zero (cf. Fig. 9). The control moment must equilibrate the moment of the force couple N, $Nl\theta_R$, for any angle θ_R to enforce a zero-frequency rotational rigid-body mode. Hence, the control moment equates to $Nl\theta_R$, and the corresponding control moment stiffness is $C_{\theta_R} = Nl$. For the controlled FE model, we find very similar eigenfrequencies. The eigenfrequencies of the SA model are slightly lower for the higher modes, due to the higher accuracy of the SA model. At this point, it is useful to compare the control moment stiffness with the one found for the FE model. In Sec. IV, we derived for two-dimensional beam elements the matrix K_{rr} and the value of the stiffness α for a beam element under compression. [Refer to Eqs. (32) and (33), respectively.] Hence, it is clear that for the uncontrolled beam $\alpha = -Nl = -2000$ N · m. The control routine will change this value to a new value α' according to the control law (44). Then we can define the control moment stiffness as

$$\alpha_{\text{ctrl}} = \alpha' - \alpha = C_{\theta_R} \tag{64}$$

For the SA solution and the FE model, we find that $C_{\theta_R} = 2000$ N · m, and, hence, $\alpha' = 0$ N · m.

In benchmark 2, there is substantial interaction of the control moment with the deformation of the beam, and all eigenfrequencies are increased significantly. The interaction of the control moment with the beam deformation is evident from the eigensolution. Again, the control moment C_{Ψ_R} must equilibrate the moment of the force couple N, $Nl\theta_R$, for any angle Ψ_R (or θ_R) to enforce a zero-frequency rotational rigid-body mode. The control moment depends on the eigenvector solution via the relation $\theta_R = \Psi_R - \mathrm{d}u/\mathrm{d}s(s = 0)$, and the control moment builds up substantial potential energy in the elastic modes and drives these mode shapes toward the shape of the next higher modes. Even in the rotational rigid-body mode there is substantial elastic deformation of the beam, but the control moment is such that, for any angle Ψ_R, there is an equilibrium position. (Total moment is zero and total potential energy is zero if an adequate control moment is chosen, similar to strain energy method for FE model.) Hence, in this case, one cannot really speak of a rotational rigid-body mode because there are substantial elastic deformations involved. However, each deformation state for this eigenvector is an equilibrium state, and, therefore, the eigenfrequency is zero.

For the SA solution, a control moment stiffness of $C_{\theta_R} = 8799$ N · m was found to obtain a zero-frequency rigid rotational mode. For the associated FE model, $C_{\theta_R} = 8958$ N · m was found using the strain energy control method. Accordingly, the new stiffness value α' equates to $\alpha' = 6799$ N · m and $\alpha = 6958$ N · m for

the SA and FE model solutions, respectively. Because the control moment for the SA solution depends on the beam flexibility via the relation (52), it is evident that an accurate representation of $du/ds(s=0)$ is required. Hence, the value n in the series expansion (54) was increased to $n=800$. In that case, a control moment stiffness of $C_{\theta_R}=8938\ \mathrm{N\cdot m}$, which matches very well with the control moment stiffness found for the FE model.

Clearly, the control system in benchmark 2 affects the bending modes to a much greater extent than the control system of benchmark 1. In benchmark 1, the sensing system, that is, the fixation to the RRF through the c-set, is chosen globally. In benchmark 2, the sensing system is chosen locally. From the results presented, it is evident that the sensing system should be chosen globally, such that the rigid motion can be sensed independently from the flexible deformation, meaning that flexible modes will hardly be affected by the control system. Hence, a one-point fixation of the beam model to the RRF should be avoided.

VII. Closed Box Tank

In this section, we will treat the example of a closed flexible box filled with fluid (Fig. 10). The fluid is subjected to earth gravity. The tank properties are given in Table 3. The aim of the analysis is to perform a free–free modal analysis and, in particular, to apply the control method as outlined in Sec. V. The example is also given as a benchmark problem in the FABE user documentation.[6] The box FE model will be ERD transformed, and the fluid mass and stiffness matrix in ERD form, generated with the boundary element method FABE, are added to the structural mass and stiffness matrix. A free–free modal analysis will be conducted without pendulum mode control, followed by the same analysis with pendulum mode control engaged. The ERD point is located in the middle of the lower tank wall, and the entire circumference of the lower tank wall is rigidly mounted to the RRF, as shown in Fig. 10. This means that the c-set DOF form a statically indeterminate set that does not allow any deformation of the lower tank wall circumference. In this example, no ullage gas is present above the fluid free surface.

Table 3 Box tank properties

Property	Value
Box edges	$0.2\times0.2\times0.25$ m
Fluid level z	0.2 m
Height of cavity above fluid level	0.05 m
Wall thickness	0.001 m
Young's modulus	70.10^{10} N/m^2
Poisson's ratio	0.3
Material density	2700 kg/m^3
Fluid density	1000 kg/m^3
Acceleration of gravity	9.81 m/s^2

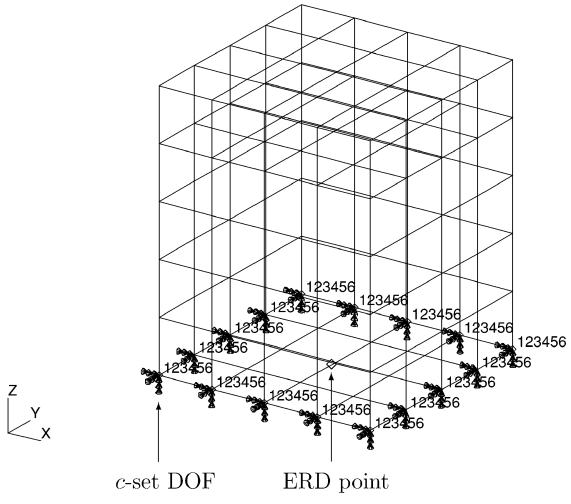

Fig. 10 Closed box tank.

Table 4 Eigenfrequencies: no control

Mode no.	Type	λ, rad^2/s^2	f, Hz
1	Rigid	0	0
2	Rigid	0	0
3	Rigid	0	0
4	Rigid	−515.3	——
5	Rigid	−515.3	——
6	Rigid	0	0
7	Fluid	220.5	2.36
8	Fluid	220.5	2.36
9	Fluid	231.9	2.42
10	Fluid	348.0	2.97
31	Structural	4.756E04	34.71
32	Structural	5.132E04	36.05
33	Structural	1.649E05	64.63

Table 5 Eigenfrequencies: controlled

Mode no.	Type	λ, rad^2/s^2	f, Hz
1	Rigid	0	0
2	Rigid	0	0
3	Rigid	0	0
4	Rigid	0	0
5	Rigid	0	0
6	Rigid	0	0
7	Fluid	231.9	2.42
8	Fluid	241.9	2.48
9	Fluid	241.9	2.48
10	Fluid	348.0	2.97
31	Structural	4.756E04	34.71
32	Structural	5.132E04	36.05
33	Structural	1.649E05	64.63

When the pendulum mode control routine is not activated, we obtain the eigenvalues and eigenfrequencies listed in Table 4. When we do activate the pendulum mode control routine, we obtain the eigenvalues and eigenfrequencies listed in Table 5. In those eigenfrequency tables, the six rigid-body modes (rigid), four sloshing modes (fluid), and the first three structural modes (structural) are tabulated. The following equations give the original stiffness matrix $\tilde{K}_{rr}$ and controlled stiffness matrix $\tilde{K}'_{rr}$:

$$\tilde{K}_{rr}=\begin{bmatrix}0&0&0&0&0&0\\0&0&0&0&0&0\\0&0&0&0&0&0\\0&0&0&-7.848&0&0\\0&0&0&0&-7.848&0\\0&0&0&0&0&0\end{bmatrix} \tag{65}$$

$$\tilde{K}'_{rr}=\begin{bmatrix}0&0&0&0&0&0\\0&0&0&0&0&0\\0&0&0&0&0&0\\0&0&0&1.325&0&0\\0&0&0&0&1.325&0\\0&0&0&0&0&0\end{bmatrix} \tag{66}$$

To conform to Eq. (64), we can write the control moment stiffness matrix $\tilde{K}_{rr_{\mathrm{ctrl}}}$ as

$$\tilde{K}_{rr_{\mathrm{ctrl}}}=\tilde{K}'_{rr}-\tilde{K}_{rr}=\begin{bmatrix}0&0&0&0&0&0\\0&0&0&0&0&0\\0&0&0&0&0&0\\0&0&0&9.173&0&0\\0&0&0&0&9.173&0\\0&0&0&0&0&0\end{bmatrix} \tag{67}$$

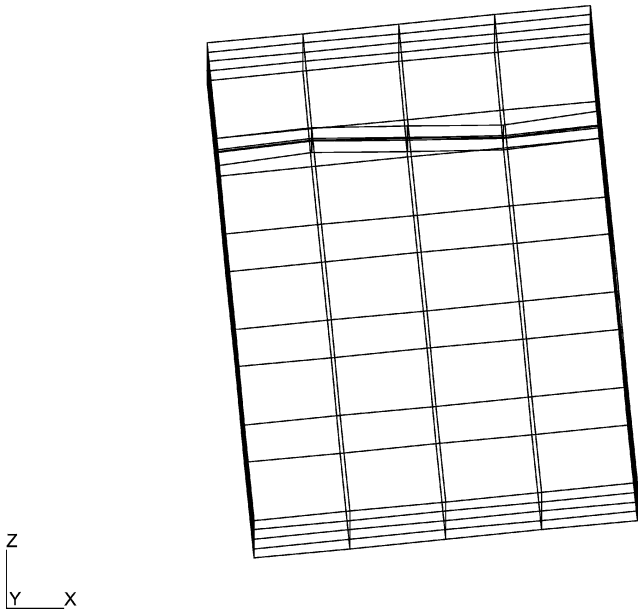

Mode 4, $\lambda = -515.4$, no control

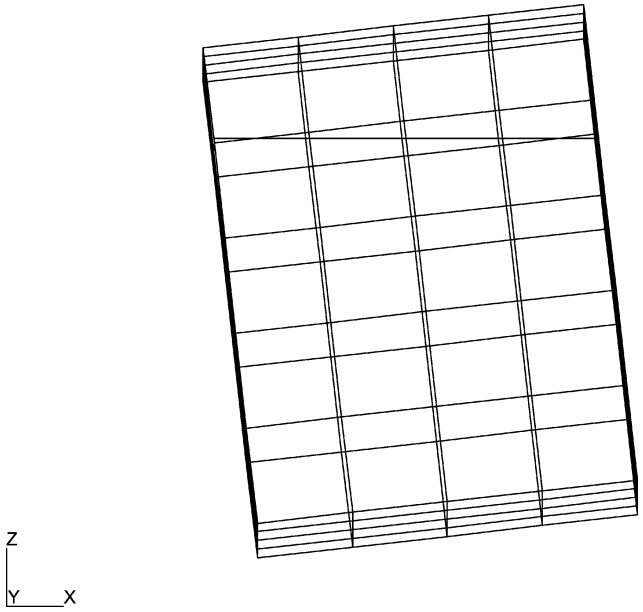

Mode 4, $\lambda = 0.0$, controlled

Fig. 11 Rotational rigid-body mode.

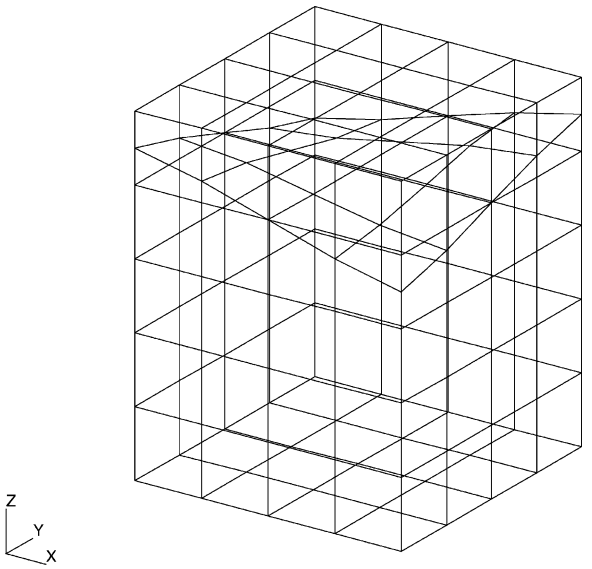

Mode 7, first sloshing, $f = 2.42$ Hz

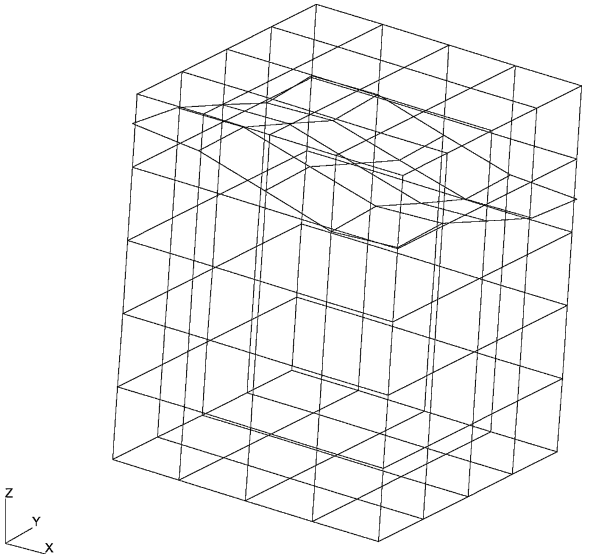

Mode 8, second sloshing, $f = 2.48$ Hz

Fig. 12 First sloshing modes, controlled.

In Fig. 11, an uncontrolled and a controlled rotational rigid-body mode are shown. Note that in the case of pendulum mode control, the fluid movement is truly rigid in the sense that the free fluid surface remains horizontal, perpendicular to the gravity vector. In Fig. 12, the first two sloshing modes and the first structural mode are shown with pendulum mode control activated. Comparison of Tables 5 and 4 shows that the sloshing modes with eigenfrequencies 2.42 and 2.97 Hz did not change, whereas the two sloshing modes with eigenfrequencies of 2.36 Hz did change to 2.48 Hz. The reason is similar to that explained in Sec. VI for the beam model prestressed by dead loads. For the tank example, the control method only affects those modes that cause a pendulum moment as a result of a shift of the fluid c.g. in the lateral direction. This can indeed be observed from the modeshapes in Fig. 12. Mode 7 does not cause a lateral shift of the c.g., whereas mode 8 does.

VIII. Ariane-5

The Ariane-5 FE model, subdivided into its substructures, is shown in Fig. 13. The Ariane-5 model shown is used for the computation of initial loads, in support of the definition of payload structures during project feasibility studies. The etage principal cryotechnique (EPC) model includes two tanks, a liquid oxygen tank on top and a liquid hydrogen tank at the bottom. The fluids, subjected to an apparent acceleration T/m, are modeled by means of the boundary element method.[6] For each substructure, the geometric stiffness due to the apparent acceleration T/m (dead loads) and the geometric stiffness matrix due to internal pressurization (follower loads) are taken into account. In the latter case, the correction matrix K^{cor} as discussed in Sec. IV.B, is taken into account by means of parameter FOLLOWK[9] available in the FE package MSC/NASTRAN. The static displacements due to the equilibrated static dead loads and pressure loads are shown in Figs. 14 and 15, respectively, for the flight event considered in this example.

Before the launcher-coupled dynamic analysis, the launcher substructures are ERD transformed by means of Eq. (2) and subsequently reduced to Craig–Bampton (CB) models.[10] For each CB model, a viscous damping matrix is computed as well. The ERD point is chosen at the center line of the EPC/upper composite interface, as shown in Fig. 13. This choice is arbitrary because the ERD point is only a reference point to describe the rigid motion. The fixation to the RRF, that is, the sensor locations (c-set DOF), have been chosen globally as shown in Fig. 13. This is in line with the findings in Sec. VI. Data recovery from the generalized solution can be accomplished in various ways by means of output transformation

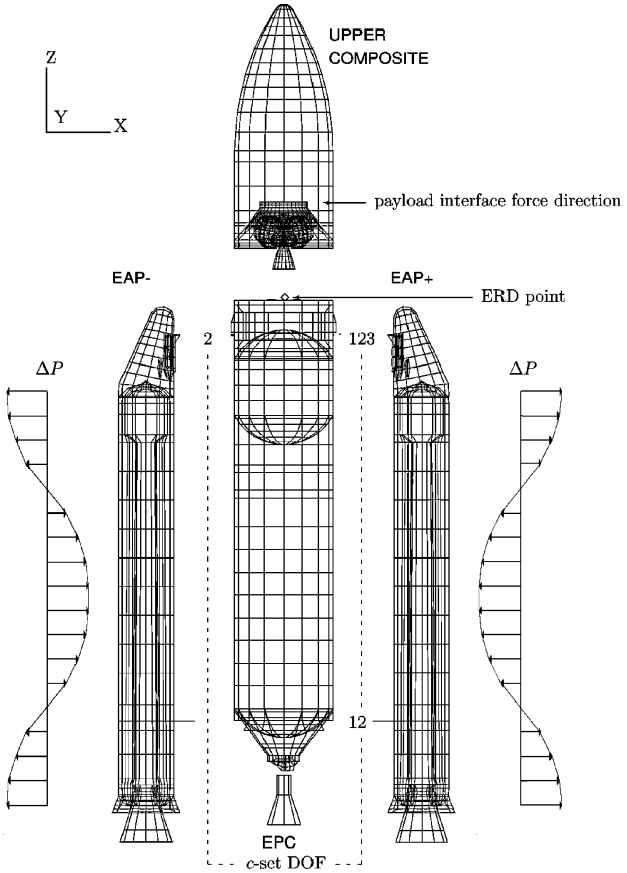

Fig. 13 Ariane-5 substructure FE models.

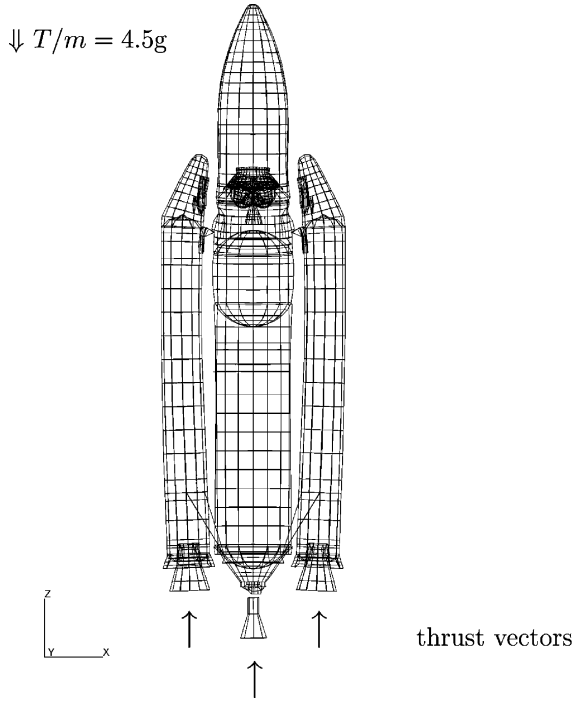

Fig. 14 Displacements due to equilibrated dead loads.

matrices (OTMs).[11] To reduce the error due to modal truncation, the modal truncation augmentation (MTA) method is used.[12] Once the reduced substructure models have been assembled into a system model, the pendulum mode control method outlined in Sec. V can be employed to enforce zero-frequency rigid-body modes. The method for pendulum mode control has been programmed into a DMAP-based[13] coupled load analysis toolbox[14] and yields the controlled stiffness matrix K'_{rr}.

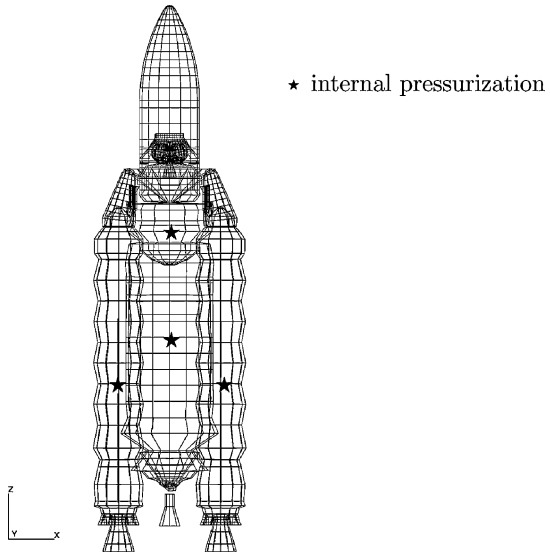

Fig. 15 Displacements due to internal pressure forces.

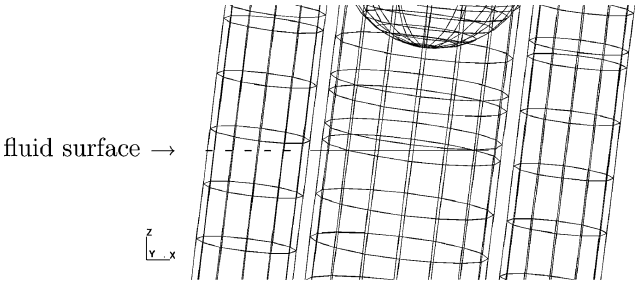

Fig. 16 Rigid-body mode, rotation about *Y* axis.

Once the matrix K'_{rr} is known, a free–free normal modes analysis can be performed, and the obtained eigenvectors can be transformed back into physical space such that the free–free mode shapes of the entire system are available. For true rigid-body behavior, the lateral rigid-body rotational modes should exhibit fluid free surfaces that are perpendicular to the gravity vector (apparent acceleration T/m). For the rotational rigid-body mode about the Y axis, this is shown in Fig. 16.

Now the model is controlled, and we can start the dynamic analysis. The load case considered will be an end-of-booster flight pressure oscillation case that occurs 110 s after the ignition of the boosters. In this load case, which is computed in the frequency domain, the response due to the booster acoustic cavity modes is studied.[15] It will be assumed that the acoustic modes in the boosters are out of phase, as shown in Fig. 13. Hence, the payload will experience a lateral excitation at its interface. The amplitude of the forces remains constant over the frequency range considered (30–54 Hz). The CB system viscous damping is a function of frequency, but on average amounts to approximately 1%. We will now study the effects of the geometric stiffness due to dead loads [thrust and gravity ($T/m = 4.5\ g$)] and follower loads (internal pressure in tanks and boosters) on the payload center point interface force in the lateral direction (x direction) as indicated in Fig. 13. In Figs. 17–19, the center point interface force response in the x direction is compared with the original response computed without prestress (K) for the following three cases: 1) prestress due to dead loads ($K + K^{g_{\text{dead}}}$), 2) prestress due to internal pressure forces ($K + K^{g_{\text{foll}}} + K^{\text{cor}}$), and 3) prestress due to the combination of pressure forces and dead loads ($K + K^{g_{\text{dead}}} + K^{g_{\text{foll}}} + K^{\text{cor}}$).

The effect of the dead loads is shown in Fig. 17. Because of the compression of the launcher structure, a small frequency shift toward a lower bending eigenfrequency causes a decrease of the resonance peak by 20%. The follower loads, the internal pressurization, has the opposite effect, as shown in Fig. 18. The structure becomes stiffer

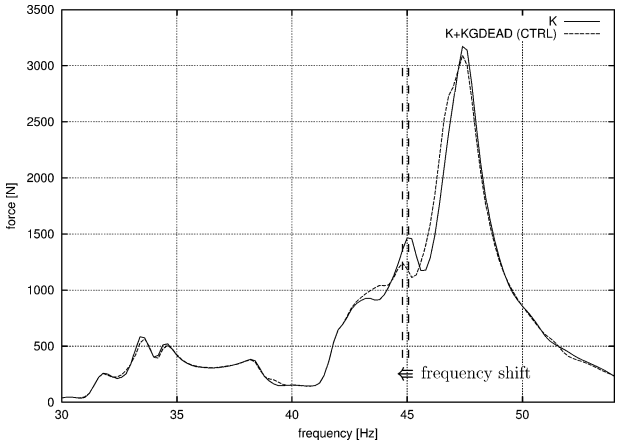

Fig. 17 Center point interface force (30–54 Hz), case 1.

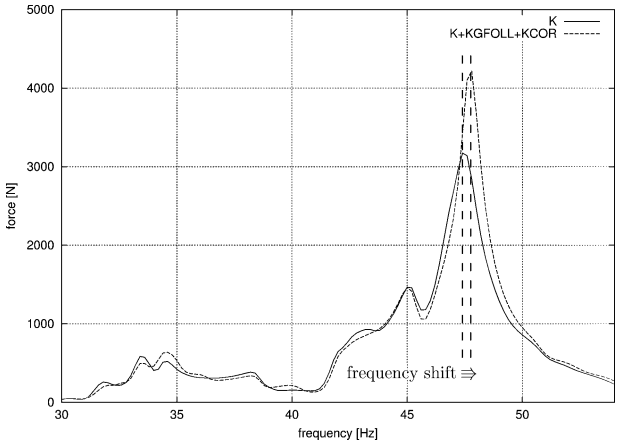

Fig. 18 Center point interface force (30–54 Hz), case 2.

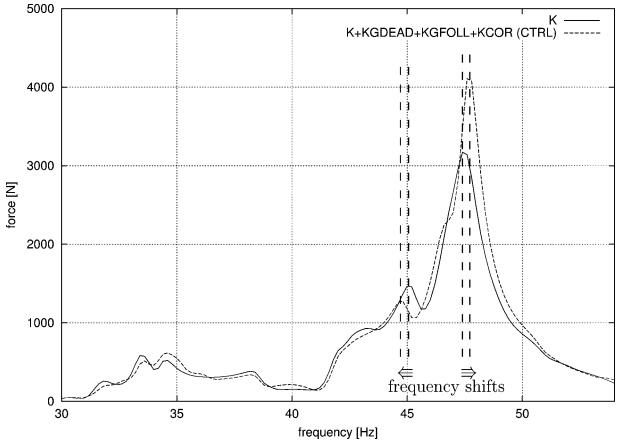

Fig. 19 Center point interface force (30–54 Hz), case 3.

and the resonance frequency is driven toward a higher frequency. In this case, the peak increases by 30%. The combined effect of prestress due to dead loads and follower loads is shown in Fig. 19. The prestress effect of the internal pressure forces is more important than the prestress effect of the equilibrated gravity loads (4.5 g) for this specific load case because the first one affects the main resonance peak. However, the dynamic effect of the gravity loads is certainly significant. The mode shape corresponding to the main resonance peak in Fig. 19 is shown in Fig. 20. The similarity between the acoustic mode (pressure distribution) in Fig. 13 and the mode shape in Fig. 20 explains the high excitation at this frequency.

In addition to the effect of prestress, we now study the effect of pendulum mode control. As shown in Fig. 21, the effect of the

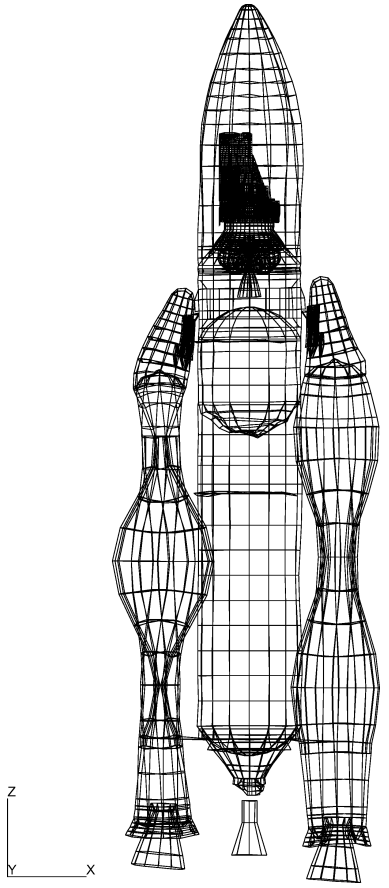

Fig. 20 Mode shape at 47.6 Hz.

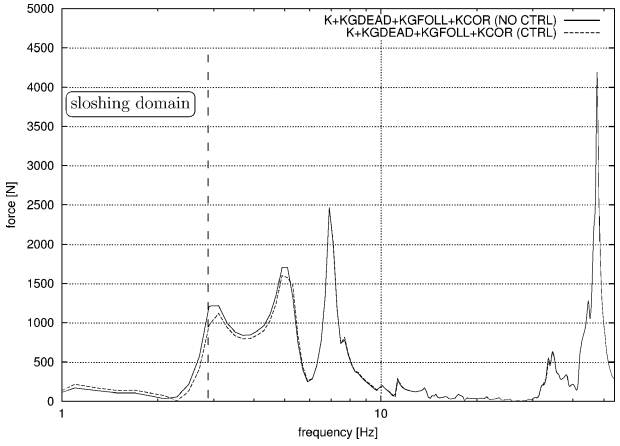

Fig. 21 Center point interface force (1–54 Hz).

pendulum mode control is small. This is according to expectation because the sensing system (fixation of launcher model to the rigid reference frame) has been chosen globally, in line with the benchmark 1 beam example in Fig. 8, Sec. VI. Some of the sloshing modes in the frequency range of 1–2.8 Hz will cause a shift of the fluid c.g. and, as a consequence, will cause a moment about the ERD point. Hence, these modes will be affected by the pendulum mode control. The low-frequency structural bending modes in the frequency range of 2.8–5 Hz will also be affected by the pendulum mode control for two reasons. The first reason is that these modes take into account the effect of the geometric stiffness due to the compressive gravitational forces. The second reason is that these bending modes interact with fluid sloshing as shown in Fig. 22. In both cases, this leads to a moment about the ERD point that is counteracted by a pendulum mode control moment. Therefore, these low-frequency bending modes are also affected by the pendulum mode control.

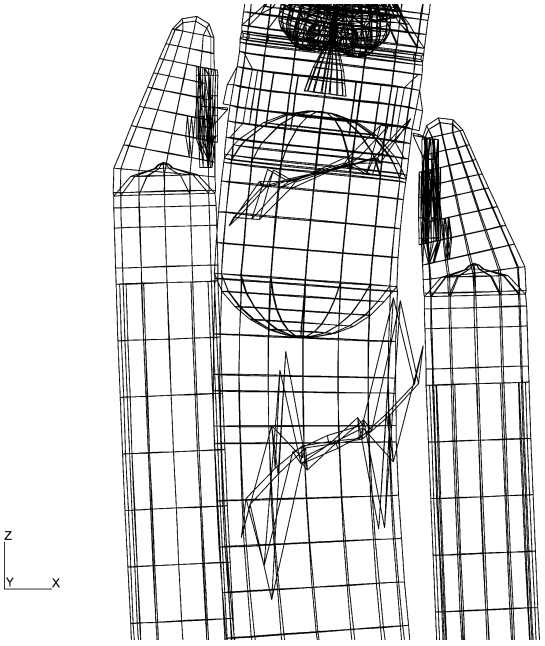

Fig. 22 Mode shape at 2.93 Hz.

IX. Conclusions

To obtain accurate results in launcher coupled dynamic analysis, the effects of prestress due to gravitational loads and internal pressure forces, and the effects of fluid sloshing in a gravity field, should be taken into account. For free–free launcher structural models, the application of geometric stiffness due to gravitational loads, and the application of fluid models defined in gravity fields, typically lead to unstable pendulum modes with negative eigenvalues.

To control such pendulum modes in a free–free launcher–payload coupled dynamic analysis, that is, to obtain zero-frequency rigid-body modes, a new control method has been developed. The control method preconditions the ERD transformed stiffness matrix such that the pendulum modes are enforced to zero-frequency rigid-body modes. For this purpose, the rigid-body forces of the rigid-body strain energy of the system is determined and set to zero by changing the stiffness at the ERD point, that is, by adding an adequate control moment stiffness.

The new pendulum mode control method is robust and cheap and yields high-quality rigid-body modes, that is, rigid-body modes with a frequency in the order of 10^{-6} Hz. For those reasons, the control method can be applied successfully in launcher–payload coupled dynamic analysis. In reality, the launcher is controlled actively by thrust vectoring or aerodynamic control forces. In addition to the control of launcher instability, this type of active control is also used to follow a specific flight path. The latter is not accomplished with the method presented.

By means of an example problem of a beam, it was concluded that the sensing system, that is, the fixation to the RRF, needs to be chosen globally to decouple the rigid rotations from the flexible motion. In that case, the effect of the control on the flexible modes remains small and is mainly found in the low-frequency modes. This has also been observed in the Ariane-5 application. Furthermore, it was found that, for the Ariane-5 example, the stiffening effect of the follower loads (internal pressure) caused a change of 30% in the main peak magnitude due to an eigenfrequency shift toward higher frequencies. The effect of increased flexibility due to the dead loads (compression due to thrust/gravity forces) caused a decrease of 20% in the second largest peak due to an eigenfrequency shift toward lower frequencies.

Acknowledgment

The first author gratefully acknowledges valuable discussions with D. J. Rixen of the Delft University of Technology.

References

[1]Kreis, A., "Control of Pendulum Modes," Technical Rept. TN-04, Kreis Consultancies, Seewis Dorf, Switzerland, 1998.

[2]Herting, D. N., and Haggenmacher, G. W., "Pressure Follower Matrix for Geometric Nonlinear Finite Element Analysis," *MSC/NASTRAN User's Conference*, MSC.Software Corp., Los Angeles, 1987.

[3]Christensen, E. R., "The Effect of Pressure Stiffness on the Dynamic Characteristics of the Advanced Solid Rocket Motor (ASRM)," AIAA Paper 91-0940, 1991.

[4]Kreis, A., and Klein, M., "On the Analysis of Liquid Filled Free–Free Tanks," ESA SP-321, European Space Research and Technology Centre, Noordwijk, The Netherlands, Oct. 1991.

[5]Ngan, I. C. S., Fransen, S. H. J. A., and Renwick, A. R., "Symmetric Fluid Structure Interaction Formulation for Compressible Media," European Conf. on Spacecraft Structures, Materials and Mechanical Testing, Centre National d'Etudes Spatiales/ESA/DLR/ASI, Toulouse, France, 2002.

[6]Kreis, A., "FABE 2.6b User Documentation," Technical Rept., Kreis Consultancies, Seewis Dorf, Switzerland, 2000.

[7]Przemieniecki, J. S., *Theory of Matrix Structural Analysis*, Dover, New York, 1985, pp. 388–391.

[8]*MSC.Nastran 2004—Quick Reference Guide*, MSC.Software Corp., Santa Ana, CA, 2003.

[9]Kilroy, K., *Quick Reference Guide—MSC.Nastran Version 2001*, MSC.Software Corp., Los Angeles, 2001.

[10]Craig, R. R., and Bampton, M. C. C., "Coupling of Substructures for Dynamic Analysis," *AIAA Journal*, Vol. 6, No. 7, 1968, pp. 1313–1319.

[11]Fransen, S. H. J. A., "An Overview and Comparison of OTM Formulations on the Basis of the Mode Displacement Method and the Mode Acceleration Method," *Worldwide Aerospace Conference and Technology Showcase*, MSC.Software Corp., Los Angeles, 2002, URL: http://www.mscsoftware.com/events/aero2002.

[12]Fransen, S. H. J. A., "A Comparison of Recovery Methods for Reduced Dynamic Substructure Models with Internal Loads," *AIAA Journal*, Vol. 42, No. 10, 2004, pp. 2130–2142.

[13]*MSC.Nastran 2004—DMAP Programmer's Guide*, MSC.Software Corp., Santa Ana, CA, 2003.

[14]Fransen, S. H. J. A., *Coupled Loads Analysis Toolbox 1.1 (Dmap Code for Use with MSC.Nastran)*, ESA/European Space Research and Technology Centre, Noordwijk, The Netherlands, 2004.

[15]Fischer, H. G., "Ariane5 Loadcases—Flight Events and Forcing Functions; Description and Methodology—Configuration 0102/0201/0202/0203," Technical Rept. TEC-MCS/2004/966/ln/HGF, issue 1, ESA/European Space Research and Technology Centre, Noordwijk, The Netherlands, 2004.

L. Peterson
Associate Editor